Fe Boltzmann temperature lidar: design, error analysis, and initial results at the North and South Poles

Xinzhao Chu, Weilin Pan, George C. Papen, Chester S. Gardner, and Jerry A. Gelbwachs

The design, development, and first measurements of a novel mesospheric temperature lidar are described. The lidar technique employs mesospheric Fe as a fluorescence tracer and relies on the temperature dependence of the population difference of two closely spaced Fe transitions. The principal advantage of this technique is that robust solid-state broadband laser source(s) can be used that enables the lidar to be deployed at remote locations and aboard research aircraft. We describe the system design and present a detailed analysis of the measurement errors. Correlative temperature observations, made with the Colorado State University Na lidar at Fort Collins, Colorado, are also discussed. Last, we present the initial range-resolved temperature measurements in the mesosphere and lower thermosphere over both the North and the South Poles obtained with this system. © 2002 Optical Society of America

OCIS codes: 280.0280, 280.3640, 120.0120, 140.0140.

1. Introduction

The middle atmosphere contains a wealth of important geophysical phenomena including the coldest part of the atmosphere—the mesopause—which occurs near 90 km; noctilucent clouds and polar mesospheric clouds, which appear near 85 km[1]; the meteoric metal layers of Na, K, Li, Ca, and Fe; the airglow layers of OH, O, and O_2; and large planetary, tidal, and gravity wave activity that plays a vital role in overall global circulation. Among remote sensing technologies employed to study the middle and upper atmosphere, lidar techniques are unique in their ability to provide high spatial and temporal resolution data on the temperature, wind, and constituent structure of this region. Currently, Na wind/temperature lidars are one of the most accurate remote-sensing instruments used to probe this region of the atmosphere.[2] Unfortunately, the demanding environmental requirements of these narrow-band Na systems generally preclude their use at remote sites or in research aircraft. For global-scale observations, the development of a robust temperature lidar is clearly attractive.

To help address this measurement need, the University of Illinois, in collaboration with The Aerospace Corporation and the National Center for Atmospheric Research (NCAR) Research Aviation Facility, has developed a robust new lidar system for measuring temperature profiles from the middle stratosphere to the lower thermosphere that can be deployed on research aircraft or operated at remote sites during both day and night. This Fe Boltzmann temperature lidar was initially deployed to the North Pole in June and July 1999 aboard the National Science Foundation (NSF)/NCAR Electra aircraft and to the South Pole in November 1999. During these campaigns the instrument made the first lidar measurements of middle-atmosphere temperatures, Fe densities, and polar mesospheric clouds over both poles during mid-summer. We describe the system design and present a detailed analysis of the measurement errors along with a comparison of temperature profiles measured by the Colorado State University Na lidar. We also present the first range-resolved temperature measurements obtained in the mesosphere and lower thermosphere over both the North and the South Poles with this new instrument.

X. Chu, W. Pan, G. C. Papen, and C. S. Gardner (cgardner@uillinois.edu) are with the Department of Electrical and Computer Engineering, University of Illinois at Urbana-Champaign, Urbana, Illinois 61801. J. A. Gelbwachs is with the Electronics and Photonics Laboratory of The Aerospace Corporation.

Received 16 August 2001; revised manuscript received 20 December 2001.

0003-6935/02/214400-11$15.00/0

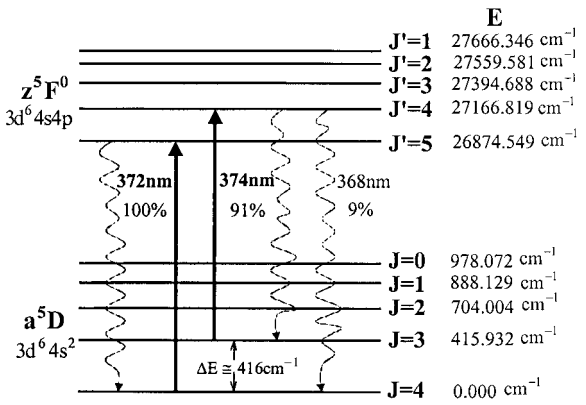

Fig. 1. Energy-level diagram of atomic Fe used for the Boltzmann technique.

2. Principle of Operation

The Fe Boltzmann temperature lidar relies on the unique energy-level distribution diagram of the ground-state manifold of Fe atoms[3] (see Fig. 1) that was first proposed by Gelbwachs for applications to lidar temperature measurements.[4] In thermal equilibrium, the ratio of the populations in the $J = 3$ and $J = 4$ sublevels in the ground-state manifold is given by the Maxwell–Boltzmann distribution law

$$\frac{P_{374}(J=3)}{P_{372}(J=4)} = \frac{\rho_{\mathrm{Fe}}(374)}{\rho_{\mathrm{Fe}}(372)} = \frac{g_2}{g_1}\exp(-\Delta E/k_B T), \quad (1)$$

where P_{372} and P_{374} are the populations in the two ground states with degeneracy factors $g_1 = 9$ and $g_2 = 7$, $\rho_{\mathrm{Fe}}(372)$ and $\rho_{\mathrm{Fe}}(374)$ are the associated Fe number densities, ΔE is the energy difference between the two levels ($\sim$416 cm^{-1}), k_B is the Boltzmann constant, and T is the atmospheric temperature. The subscripts 372 and 374 refer to the excitation wavelengths of two transitions in nanometers (actually, $\lambda_{372} = 372.0993$ nm and $\lambda_{374} = 373.8194$ nm). The line parameters for these two transitions are summarized in Table 1. At 200 K, the ratio of the populations is approximately 26. The temperature is then given by

$$T = \frac{\Delta E/k_B}{\ln\left[\dfrac{g_2}{g_1}\dfrac{\rho_{\mathrm{Fe}}(372)}{\rho_{\mathrm{Fe}}(374)}\right]}. \quad (2)$$

The Fe densities in these two states can be measured with resonance fluorescence lidar techniques. The densities are proportional to the number of backscattered photon counts from Fe atoms (N_{Fe}) detected for each wavelength probed by the lidar. The detected Fe photon count is given by the lidar equation[5]

$$N_{\mathrm{Fe}}(\lambda, z) = \left[\frac{P_L \Delta t T_a}{hc/\lambda} E(\lambda, z)\right]\sigma_{\mathrm{eff}}(\lambda, T, \sigma_L) R_{B\lambda} \times \rho_{\mathrm{Fe}}(\lambda, z)\Delta z\left[E(\lambda, z) T_a \frac{A_R}{4\pi z^2}\eta\right], \quad (3)$$

where z is the altitude; P_L is power of the laser; Δt is the temporal resolution; Δz is the vertical resolution; T_a is the one-way transmittance of the lower atmosphere; λ is the wavelength; c is the vacuum speed of light; h is Planck's constant; $E(\lambda, z)$ is the extinction coefficient of the signal associated with Fe absorption; $\sigma_{\mathrm{eff}}(\lambda, T, \sigma_L)$ is the effective absorption cross section of the Fe transition, which is a function of temperature T, laser wavelength λ and laser linewidth σ_L; $R_{B\lambda}$ is the branching ratio ($R_{B374} = 0.9114$, $R_{B372} = 1$)[6]; A_R is the area of the receiving telescope; and η is the overall optical efficiency of the system. The effect of the radial velocity on the absorption cross section has not been included, but it is negligible for zenith observations.[7] The total detected signal also includes the background noise count $N_B(\lambda, z)$, which must be added to the Fe signal count given by Eq. (3).

The current system uses two separate lasers and receivers because the two Fe lines are too far apart in wavelength for us to probe easily by tuning a single laser, yet they are too close to be separated in the receiving telescope by use of a dichroic beam splitter. To compensate for signal variations in each of these systems, we normalize the photon counts from the Fe layer at each wavelength by the Rayleigh counts (N_R) over a common lower altitude range, typically near 50 km,

$$N_R(\lambda, z_R) = \left(\frac{P_L \Delta t T_a}{hc/\lambda}\right)\sigma_R(\lambda)\rho_{\mathrm{atmos}}(z_R)\Delta z \times \left(T_a \frac{A_R}{4\pi z_R^2}\eta\right), \quad (4)$$

where z_R is the normalization altitude, $\rho_{\mathrm{atmos}}(z_R)$ is the atmospheric number density at the normalization altitude, and $\sigma_R(\lambda)$ is the effective atmospheric Rayleigh backscatter cross section that is 4π times of Rayleigh angular backscatter cross section $\sigma_R(\theta = \pi)$, i.e., $\sigma_R(\lambda) = 4\pi\sigma_R(\theta = \pi)$, where θ is the scattering angle. The product of the atmospheric number density and the effective Rayleigh backscatter cross section can be expressed as[5]

$$\sigma_R(\lambda)\rho_{\mathrm{atmos}}(z_R) = 1.370 \times 10^{-30} \times \frac{273}{T(z_R)}\frac{P(z_R)}{1013}\frac{1}{\lambda^{4.0117}}, \quad (5)$$

where $T(z_R)$ is the atmospheric temperature in degrees Kelvin, $P(z_R)$ is the atmospheric pressure in millibars, and λ is the laser wavelength in meters.

Table 1. Fe Resonance Line Parameters

Transition Wavelength	372.0993 nm	373.8194 nm
Degeneracy	$g_1 = 9$	$g_2 = 7$
Oscillator Strength	0.0414	0.0382
Branching Ratio	1	0.9114

The Rayleigh normalized, background-corrected Fe signal count is defined as

$$N_{\mathrm{norm}}(\lambda, z) = \frac{N_{\mathrm{Fe}}(\lambda, z) + N_B(\lambda, z) - \hat{N}_B(\lambda)}{N_R(\lambda, z_R) + N_B(\lambda, z_R) - \hat{N}_B(\lambda)} = \frac{z_R{}^2 E^2(\lambda, z) R_{B\lambda} \sigma_{\mathrm{eff}}(\lambda, T, \sigma_L) \rho_{\mathrm{Fe}}(\lambda, z)}{z^2 \sigma_R(\lambda) \rho_{\mathrm{atmos}}(z_R)}, \quad (6)$$

where $\hat{N}_B(\lambda)$ is the estimated background noise count. By use of Eq. (1), the ratio of the normalized Fe signal counts at the two wavelengths (R_T) can be related to temperature:

$$\begin{aligned} R_T(z) &= \frac{N_{\mathrm{norm}}(\lambda_{374}, z)}{N_{\mathrm{norm}}(\lambda_{372}, z)} \\ &= \frac{g_2}{g_1} \frac{R_{B374}}{R_{B372}} \left(\frac{\lambda_{374}}{\lambda_{372}} \right)^{4.0117} \frac{E^2(\lambda_{374}, z)}{E^2(\lambda_{372}, z)} \\ &\quad \times \frac{\sigma_{\mathrm{eff}}(\lambda_{374}, T, \sigma_{L374})}{\sigma_{\mathrm{eff}}(\lambda_{372}, T, \sigma_{L372})} \exp(-\Delta E / k_B T) \\ &= 0.7221 R_E{}^2(z) R_\sigma \exp(-598.44/T), \end{aligned} \quad (7)$$

where

$$R_E(z) = \frac{E(\lambda_{374}, z)}{E(\lambda_{372}, z)}, \quad (8)$$

$$R_\sigma = \frac{\sigma_{\mathrm{eff}}(\lambda_{374}, T, \sigma_{L374})}{\sigma_{\mathrm{eff}}(\lambda_{372}, T, \sigma_{L372})}. \quad (9)$$

At 200 K the 372-nm Fe signal is approximately 30 times stronger than the 374-nm signal so that $R_T \sim 1/30$. By solving Eq. (7) for temperature, we obtain the final result of

$$\begin{aligned} T(z) &= \frac{\Delta E / k_B}{\ln\left[\frac{g_2}{g_1} \frac{R_{B374}}{R_{B372}} \left(\frac{\lambda_{374}}{\lambda_{372}} \right)^{4.0117} \frac{R_E{}^2(z) R_\sigma}{R_T(z)} \right]} \\ &= \frac{598.44}{\ln\left[\frac{0.7221 R_E{}^2(z) R_\sigma}{R_T(z)} \right]} \text{ (K)}. \end{aligned} \quad (10)$$

Thus, by measuring the Fe signal level at the two wavelengths and computing $R_T(z)$ using Eqs. (6) and (7), one can derive the temperature from Eq. (10), provided that the ratios of the extinction and the effective backscatter cross sections are known.

3. System Design

A schematic of the system is shown in Fig. 2. The system contains two laser transmitters and two optical receivers. Each laser transmitter consists of an injection-seeded, frequency-doubled, flashlamp-pumped alexandrite laser (Light Age, Inc., Model PAL 101). The injection seeder laser is a commercial tunable external cavity diode laser [formerly EOSI, Inc. (Newport), Model 2010]. The wavelength control of the seeder laser is accomplished via a Burleigh wavemeter (Model WA-1500) that has a frequency accuracy of ±40 MHz at the fundamental wavelengths of 744 and 748 nm. This corresponds to a frequency accuracy of ±80 MHz when the lasers are frequency doubled to probe the Fe fluorescence lines. Each seeder laser wavelength is sequentially monitored with a computer-controlled flip mirror. The wavelength is adjusted via a software control loop. The elliptical output of the external cavity laser is corrected by use of an anamorphic prism pair, and then the circularized output is fiber coupled for injection into the main laser cavity. The fiber coupling allows flexibility in locating the seeder lasers with respect to the alexandrite lasers.

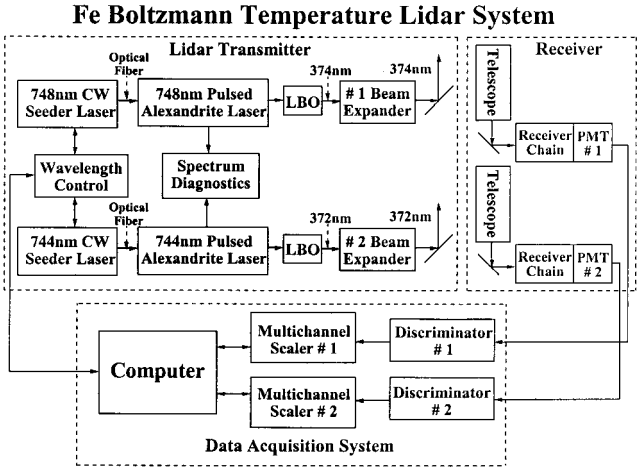

Fig. 2. Diagram of the Fe Boltzmann temperature lidar system. LBO, lithium triborate crystal; PMT, photomultiplier tube.

The frequency-doubled output of the alexandrite laser is expanded to decrease the divergence to approximately 350 μrad to enable daytime operation. The pulsed output of the alexandrite laser is monitored with a commercial pulsed laser spectrum analyzer (Burleigh Instruments, Inc., Model RFP-3600). The pulsed output is not a single frequency but consists of 3–4 modes within a frequency range of approximately 800 MHz. The effective cross section of each Fe transition is determined by the scanning of the wavelength of each laser through the Fe transition with the atmospheric returns. This will be discussed in detail in Section 4.

Each optical receiver includes a commercial Meade 0.4-m LX200 Schmidt–Cassegrain telescope with custom coatings to enhance UV transmission. The field of view of the telescope is controlled via a pinhole at the focal plane and is set to match the outgoing divergence of the laser. A mechanical chopper is placed close to the focal plane to enable blanking of the low-altitude laser returns. The return signal is collimated and passed through an interference filter and a pressure-tuned, temperature-stabilized Fabry–Perot etalon before being detected by a photon-counting photomultiplier tube. The output signal from the photomultiplier tube is then thresholded by use of a discriminator, and the photon counts are

Table 2. System Parameters for Fe Boltzmann Temperature Lidar

Characteristics	Channel 1 (374 nm)	Channel 2 (372 nm)
Lidar Transmitter		
Alexandrite Laser	Light Age, Inc., Model PAL 101 Frequency-Doubled Pulsed Alexandrite Laser	
Linewidth (FWHM) (MHz)	864	876
Pulse energy (mJ)	100	100
Pulse length (ns)	55–65	55–65
Repetition rate (Hz)	33.2	34.1
Average power (W)	3	3
Beam divergence (mrad)	0.35	0.35
Injection Seeder Laser	Formerly EOSI, Inc., (Newport) Model 2010 External Cavity Diode Laser	
Wavelength (nm)	747.6390	744.1990
Output power (mW)	3	3
Linewidth (MHz) (50 ms)	<100 kHz	<100 kHz
Lidar Receiver		
Characteristics	Nighttime	Daytime
Telescope	Meade, Model LX200 (f/10) 0.4064-m-Diameter Schmidt–Cassegrain Design	
Aperture area (m^2)	0.130	0.130
Telescope focal length (mm)	4064	4064
Field of view (mrad)	1	0.5
Interference filter bandwidth (nm)	4.2	0.3
Etalon bandwidth (GHz)	—	30
Photomultiplier tube quantum efficiency	28%	28%
Receiver optical efficiency	58.7%	18.0%
Total receiver efficiency	16.4%	5.0%

integrated by use of a multichannel scaler. A list of the system parameters is given in Table 2. Compared with narrow-band Na systems, the Fe density at 372 nm is, on average, approximately a factor of 2 higher than that of Na,[8] and the effective cross section is approximately an order of magnitude lower than that of Na. Thus the average power required to produce an Fe signal count at 372 nm that is comparable with the Na signal count is roughly a factor of 5 higher for Fe, assuming equal efficiencies for the rest of the system.

4. Error Analysis

There are two major sources of error, namely, fluctuations in the signal levels associated with photon noise and fluctuations in the effective backscatter cross sections associated with laser tuning errors and laser linewidth fluctuations. The extinction is calculated from the measured Fe densities and temperatures and also includes errors. However, the two-way extinction correction is typically no more than approximately 1%–2% at the top of the 372-nm Fe layer and much less than a percent for the 374-nm Fe layer. For this reason, extinction errors are small and can be neglected. Because the laser tuning errors and linewidth fluctuations are uncorrelated with signal photon noise, by use of $\Delta T = (\partial T/\partial R_T)\Delta R_T + (\partial T/\partial R_\sigma)\Delta R_\sigma$, the total rms temperature error can be derived from Eq. (10) as

$$\Delta T_{\mathrm{rms}} = \frac{T^2}{\Delta E/k_B}\left[\left\langle\left(\frac{\Delta R_T}{R_T}\right)^2\right\rangle + \left\langle\left(\frac{\Delta R_\sigma}{R_\sigma}\right)^2\right\rangle\right]^{1/2}. \quad (11)$$

Because $\Delta E/k_B \sim 600$ K and T is in the range of 150–250 K, the total relative error for both R_T and R_σ in Eq. (11) must be no larger than 1.5% for a ± 1 K accurate temperature measurement at $T = 200$ K. We now consider each of these two error sources separately.

The total effective backscatter cross section is proportional to the effective absorption cross section:

$$\sigma_{\mathrm{eff}}(\lambda, T, \sigma_L) = \sigma_{\mathrm{effabs}}(\lambda, T, \sigma_L). \quad (12)$$

We have accounted for the decay of the excited state to multiple ground states by including the appropriate branching ratios in the lidar equation. The effective absorption cross section is the convolution of the atomic absorption cross section and laser line shape:

$$\sigma_{\mathrm{eff}}(\lambda, T, \Delta\nu, \sigma_L) = \int_{-\infty}^{+\infty} \sigma_{\mathrm{abs}}(\nu', \lambda_0, T) \times g_L(\nu', \lambda, \sigma_L)\mathrm{d}\nu', \quad (13)$$

where $\sigma_{abs}(\nu', \lambda_0, T)$ is the intrinsic atomic absorption cross section centered at wavelength λ_0, $g_L(\nu', \lambda, \sigma_L)$ is the normalized laser line shape centered at wavelength λ, ν' is the frequency, and $\Delta\nu$ is the frequency difference between the Fe line center λ_0 and laser line center λ. Assuming a Gaussian functional form for both the laser line shape and the absorption cross section, the effective cross section is

$$\sigma_{eff}(\lambda, T, \Delta\nu, \sigma_L) = \frac{1}{\sqrt{2\pi}\sigma_\lambda} \frac{e^2}{4\epsilon_0 m_e c} f_\lambda \exp\left(-\frac{\Delta\nu^2}{2{\sigma_\lambda}^2}\right), \tag{14}$$

where f_λ is the oscillator strength of the transition ($f_{372} = 0.0414$ and $f_{374} = 0.0382$), ϵ_0 is the permitivity of free space, e is the charge of an electron, m_e is the mass of the electron, c is the velocity of light, and

$$\sigma_\lambda = \sqrt{{\sigma_D}^2 + {\sigma_L}^2}, \tag{15}$$

where σ_D is the rms Doppler width of the intrinsic atomic absorption cross section,

$$\sigma_D = \frac{1}{\lambda}\left(\frac{k_B T}{m_{Fe}}\right)^{1/2}, \tag{16}$$

and m_{Fe} is the mass of an Fe atom.

In practice, we tune the lasers to the peaks of the Fe lines so that uncertainties in the assumed values for the cross section arise because of tuning errors ($\Delta\nu$) and uncertainties in the assumed values for the laser linewidths ($\Delta\sigma_L$). The ratio of the cross sections is given by

$$R_\sigma = 0.9227 \frac{\sigma_{372}}{\sigma_{374}} \exp\left(\frac{{\Delta\nu_{372}}^2}{2{\sigma_{372}}^2} - \frac{{\Delta\nu_{374}}^2}{2{\sigma_{374}}^2}\right). \tag{17}$$

Although temperature is required to evaluate the Doppler linewidths, the cross-section ratio is insensitive to temperature so that errors in R_σ associated with errors in assumed temperature are negligible. Because the lasers are identical and the wavelength difference is small, we assume the laser linewidths are similar so that σ_{372} is approximately equal to σ_{374}. In this case, the cross-section ratio can be simplified to

$$R_\sigma \cong \begin{cases} 0.9270\left[1 + \dfrac{({\sigma_{L372}}^2 - {\sigma_{L374}}^2)}{{\sigma_\lambda}^2}\right]^{1/2} \\ \quad \times \exp\left[\dfrac{({\Delta\nu_{372}}^2 - {\Delta\nu_{374}}^2)}{2{\sigma_\lambda}^2}\right], \qquad \sigma_L \ll \sigma_D \\ 0.9227\left[1 + \dfrac{({\sigma_{L372}}^2 - {\sigma_{L374}}^2)}{{\sigma_\lambda}^2}\right]^{1/2} \\ \quad \times \exp\left[\dfrac{({\Delta\nu_{372}}^2 - {\Delta\nu_{374}}^2)}{2{\sigma_\lambda}^2}\right], \qquad \sigma_D \ll \sigma_L \end{cases}. \tag{18}$$

If both the laser linewidths and the squares of the tuning errors are identical, then $0.9227 < R_\sigma < 0.9270$. For identical lasers, the cross-section ratio varies less than 0.5% as the laser linewidth varies from zero to infinity. Because the cross-section ratio is insensitive to the absolute value of the laser linewidths when they are approximately equal, it is more important to know the linewidth difference rather than the absolute values of the individual linewidths. We can express the relative error in the cross-section ratio in terms of the laser tuning errors and uncertainties in the assumed values for the laser linewidths or in terms of the linewidth difference:

$$\frac{\Delta R_\sigma}{R_\sigma} \cong \begin{cases} \dfrac{|{\Delta\nu_{372}}^2 - {\Delta\nu_{374}}^2|}{2{\sigma_\lambda}^2} \\ \sqrt{2}\left(\dfrac{\sigma_L}{\sigma_\lambda}\right)^2 \dfrac{\Delta\sigma_L}{\sigma_L} \\ \left(\dfrac{\sigma_L}{\sigma_\lambda}\right)^2 \dfrac{|\sigma_{L372} - \sigma_{L374}|}{\sigma_L} \end{cases}. \tag{19}$$

By combining expression (19) with Eq. (11), we obtain

$$\Delta T_{rms}(K) \cong \begin{cases} \pm \dfrac{T^2}{2(\Delta E/k_B)} \dfrac{|{\Delta\nu_{372}}^2 - {\Delta\nu_{374}}^2|}{{\sigma_\lambda}^2} \\ \pm \dfrac{\sqrt{2}T^2}{(\Delta E/k_B)}\left(\dfrac{\sigma_L}{\sigma_\lambda}\right)^2 \dfrac{\Delta\sigma_L}{\sigma_L} \\ \pm \dfrac{T^2}{(\Delta E/k_B)}\left(\dfrac{\sigma_L}{\sigma_\lambda}\right)^2 \dfrac{|\sigma_{L372} - \sigma_{L374}|}{\sigma_L} \end{cases}. \tag{20}$$

To compute the effective cross sections from Eq. (14) or their ratio from Eq. (17), we need to determine σ_λ for each line. This is done by scanning the lasers through the Fe fluorescence lines and recording the atmospheric returns as a function of frequency. A Gaussian function of frequency is fitted to the normalized signal counts to determine the total rms linewidths. The laser linewidths are computed from Eqs. (15) and (16). Plotted in Fig. 3 is an example fit to 372-nm data. The results for the cross section

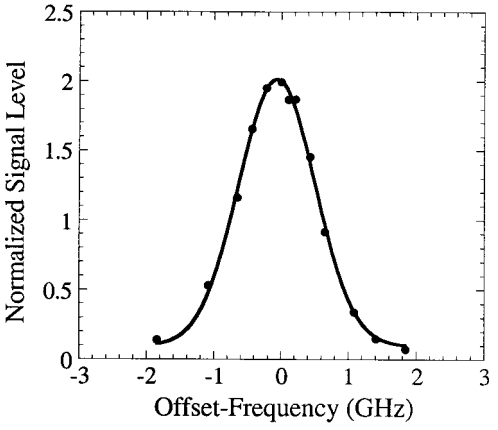

Fig. 3. Plot of the effective backscatter cross section spectrum for the Fe 372-nm line obtained by the scanning of the lidar frequency and observation of the returns from the mesospheric Fe layer.

Table 3. Measured Cross Sections and Laser Parameters

Parameter	372-nm System	374-nm System
$\sigma_\lambda \pm \Delta\sigma_\lambda$ (MHz)	566.8 ± 16.7	562.1 ± 20.0
σ_D (MHz) at $T = 170$ K	427.7	425.7
$\Delta\nu \pm \delta(\Delta\nu)$ (MHz)	59.7 ± 10.8	82.2 ± 13.8
$\sigma_L \pm \Delta\sigma_L$ (MHz)	371.9 ± 25.4	367.0 ± 30.7
$\sigma_{\text{eff}} \pm \Delta\sigma_{\text{eff}}$ ($\times 10^{-12}$ cm^2)	0.770 ± 0.023	0.718 ± 0.026
$\Delta\sigma_\lambda/\sigma_\lambda$	2.95%	3.56%
$\Delta\sigma_L/\sigma_L$	6.83%	8.37%
$\Delta\sigma_{\text{eff}}/\sigma_{\text{eff}}$	2.99%	3.62%

and laser parameters and the statistical errors of the fits are listed in Table 3.

There are two ways to determine the cross-section ratio and the errors. The cross sections can be computed from the laser scans with Eq. (14). In this case the relative error in the cross-section ratio is given by

$$\frac{\Delta R_\sigma}{R_\sigma} = \left[\left(\frac{\Delta\sigma_{\text{eff}}(372)}{\sigma_{\text{eff}}(372)}\right)^2 + \left(\frac{\Delta\sigma_{\text{eff}}(374)}{\sigma_{\text{eff}}(374)}\right)^2\right]^{1/2}. \quad (21)$$

By use of the data in Table 3, the cross-section ratio is 0.9325, and the relative error is 4.7%, which, according to Eq. (11), yields an error of approximately ±3.1 K at $T = 200$ K. Alternatively, we can assume the laser linewidths are identical and that both lasers are tuned to the peaks of the fluorescence lines. In this case the cross-section ratio is assumed to be 0.9270 when $\sigma_L \ll \sigma_D$ or 0.9227 when $\sigma_D \ll \sigma_L$ [see expression (18)]. In our case in which both laser linewidths are approximately 370 MHz and do not satisfy either extreme, the assumed value of the cross-section ratio would be 0.9252 [see Eq. (17)]. According to the linewidth scan data in Table 3, tuning errors are comparable with the ±80-MHz accuracy of the Burleigh wavemeter at the frequency-doubled UV lines. Tuning errors would introduce a relative error of less than 1% in the cross-section ratio, which corresponds to a temperature error of ±0.7 K. Uncertainties in the laser linewidths (25 and 31 MHz) introduce a temperature error of ±3.1 K. Alternatively, if the laser linewidths are similar, we can use the linewidth difference to compute the temperature error rather than the uncertainties of the measured values. The laser linewidths differ by 4.9 ± 40 MHz. If we assume the laser linewidth difference is no larger than the uncertainty in the measured difference (40 MHz), then the relative cross-section error is less than 4.6%, which corresponds to a temperature error of ±3.1 K. If the actual linewidth difference were assumed to be the measured value of 4.9 MHz, then the temperature error would be approximately ±0.4 K.

The impact of photon noise is calculated by use of the same analysis for the Na lidar technique in which winds and temperatures are determined by computation of the ratio of normalized photon counts obtained at several frequencies within the Na D_2 fluorescence line. Because the Fe signals are normalized by the strong Rayleigh signal at lower altitudes near 50 km, the photon noise contributed by the Rayleigh signal is negligible. The dominant error source is photon noise contributed by the weaker 374-nm Fe channel. If we assume the Rayleigh normalizing signals for the 372- and 374-nm channels are comparable, the temperature ratio R_T is given approximately by

$$R_T \cong \frac{N_{\text{Fe}}(374, z) + N_B(374, z) - \hat{N}_B(374)}{N_{\text{Fe}}(372, z) + N_B(372, z) - \hat{N}_B(372)}. \quad (22)$$

The rms relative error in the temperature ratio associated with photon noise is easily calculated from expression (22) by recognition that the Fe signal and background counts are uncorrelated Poisson-distributed random numbers. If we assume that the mean background counts on the 372- and 374-nm channels are approximately equal and $T = 200$ K so that $1/R_T \sim 30$, the rms relative error is given by

$$\left[\left\langle\left(\frac{\Delta R_T}{R_T}\right)^2\right\rangle\right]^{1/2} = \frac{(1 + 1/R_T)^{1/2}}{[N_{\text{Fe}}(372, z)]^{1/2}} \times \left[1 + \frac{(1 + 1/R_T{}^2)}{(1 + 1/R_T)}\frac{1}{\text{SBR}_{372}}\right]^{1/2} \approx \frac{5.6}{[N_{\text{Fe}}(372, z)]^{1/2}}\left(1 + \frac{29}{\text{SBR}_{372}}\right)^{1/2}, \quad (23)$$

where the signal-to-background ratio is

$$\text{SBR}_{372} = \frac{N_{\text{Fe}}(372, z)}{\hat{N}_B(372)}. \quad (24)$$

By substituting expression (23) into Eq. (11), the rms temperature error associated with photon noise at $T = 200$ K is

$$\Delta T_{\text{rms}}(K) = \frac{\pm 372}{[N_{\text{Fe}}(372, z)]^{1/2}}\left(1 + \frac{29}{\text{SBR}_{372}}\right)^{1/2}. \quad (25)$$

At night when SBR_{372} is large, approximately 140,000 Fe signal counts are required in each resolution cell of the stronger 372-nm channel to achieve a temperature accuracy of ±1 K. This requirement drops to approximately 15,000 counts for an accuracy of ±3 K. During daytime when SBR_{372} can be much less than 1, the signal requirements increase substantially. For example if $\text{SBR}_{372} = 1$, the required signal level is 4×10^6 counts for ±1-K accuracy. Long averaging times, typically several hours, are required to obtain accurate temperature measurements during the daytime. The error budget for the Fe Boltzmann lidar is summarized in Table 4.

5. Rayleigh Temperature Retrievals

Above the stratospheric aerosol layers and below the Fe layer, the received signal results from pure molecular scattering. Molecular scattering is proportional to the atmospheric density, and the temperature profile can be derived from the relative atmospheric density profile by use of the Rayleigh

Table 4. Fe Boltzmann Lidar Error Budget for $T = 200$ K and $\sigma_L = 370$ MHz

Parameter	Temperature Error (K)	Value for $\Delta T_{\mathrm{rms}} = \pm 1$ K
Laser tuning errors $\Delta\nu$	$\pm 33 \dfrac{\lvert \Delta\nu_{372}{}^2 - \Delta\nu_{374}{}^2 \rvert}{\sigma_\lambda{}^2}$	100 MHz
Laser linewidth errors $\Delta\sigma_L$	$\pm 95 \left(\dfrac{\sigma_L}{\sigma_\lambda}\right)^2 \dfrac{\Delta\sigma_L}{\sigma_L}$	9 MHz
Laser linewidth difference $\lvert\sigma_{L372} - \sigma_{L374}\rvert$	$\pm 67 \left(\dfrac{\sigma_L}{\sigma_\lambda}\right)^2 \dfrac{\lvert\sigma_{L372} - \sigma_{L374}\rvert}{\sigma_L}$	13 MHz
Signal level $N_{\mathrm{Fe}}(372, z)$	$\pm \dfrac{372}{[N_{\mathrm{Fe}}(372, z)]^{1/2}} \left(1 + \dfrac{29}{\mathrm{SBR}_{372}}\right)^{1/2}$	1.8×10^5 at $\mathrm{SBR}_{372} = 100$ 4.2×10^6 at $\mathrm{SBR}_{372} = 1$

lidar technique.[5] This involves integrating the relative density profile downward by use of a starting temperature at the highest altitude in combination with the hydrostatic equation and the ideal gas law. Most middle atmosphere Rayleigh lidars employ frequency-doubled Nd:YAG lasers operating at 532 nm in the green region of the visible spectrum. Typical systems employ telescopes with diameters near 1 m and lasers with average powers levels in the 10–15-W range. These systems have power aperture products of approximately 10 Wm^2. The Fe Boltzmann lidar operates in the near UV in which Rayleigh scattering is more than four times stronger than at 532 nm. By combination of the molecular (Rayleigh) scattered signal from the 372- and 374-nm channels, temperatures can be derived from approximately 30 km to approximately 75 km with the Rayleigh technique. The Fe Boltzmann temperature at the bottom of the Fe layer near 80 km, rather than a model estimate, can be used as the starting temperature for the retrieval. For our system, which employs two 3-W lasers and two 0.4-m diameter telescopes, the equivalent power aperture product at 532 nm is approximately 3 Wm^2. Thus the Fe system can derive temperature profiles with an accuracy and vertical resolution comparable with many existing Rayleigh lidars if the signals are integrated approximately three times longer.

6. Comparison with the Colorado State University Na Lidar

The physics that forms the basis of the Fe Boltzmann temperature lidar technique is well established. The spectroscopy of the Fe atom is well understood from quantum-mechanical principles and from laboratory measurements. There is no doubt that accurate temperature measurements can be made with this technique, provided that the lidar data are processed properly and the key system parameters are accurately characterized. The crucial parameters are the effective backscatter cross sections of the 372- and 374-nm Fe lines or, equivalently, the laser linewidths. Although the system includes a pulse spectrum analyzer to monitor the IR output spectra of the alexandrite lasers to ensure adequate seeding (see Fig. 2), during routine operation the linewidths are calibrated by the scanning of both lasers through the Fe resonance lines and observation of the atmospheric returns. Because this process is time consuming, it is not done during every observation period. Airborne measurements present the most challenging operational environment for the instrument. Vibrations from the engines and from turbulence and temperature fluctuations in the cabin all have the potential for affecting the laser tuning and seeding. Our ground-based calibration measurements suggest that the laser linewidths are stable and nominally near 370 MHz when the lasers are properly adjusted. To determine if these values are also applicable to airborne observations, we compared airborne temperature measurements made near Fort Collins, Colorado, with similar measurements made with the Colorado State University (CSU) Na lidar.

The Fe lidar was first deployed on the NSF/NCAR Electra aircraft to make observations of meteor trails over Okinawa during the 1998 Leonid meteor shower.[9] During this campaign, only Fe density data were collected. In June and July 1999 the lidar system was again deployed on the NSF/NCAR Electra to make temperature and Fe density observations over the north polar cap during the Arctic Mesopause Temperature Study (AMTS). This study began on 16 June with a ferry flight from Broomfield, Colorado (40 °N, 105 °W) to Resolute Bay, Canada (75 °N, 95 °W), where the campaign was based. One round-trip flight was made to Sondrestromfjord, Greenland (67 °N, 50 °W) on 19 June, and four flights were made to the geographic North Pole on 21 June, 1 July, 2 July, and 4 July. On 5 July the system was flown to Anchorage, Alaska (61 °N, 150 °W), and one additional flight was made on 8 July to probe noctilucent clouds (NLCs) over the Gulf of Alaska.

During the return ferry flight from Anchorage to Broomfield on 9 July, the flight path passed near Fort Collins, Colorado, where the CSU group was also making mesopause-region temperature measurements during that night with a narrow-band Na lidar. The flight path is illustrated in Fig. 4. The weather at Fort Collins was partly cloudy, and so data collection was sporadic. The average temperature profile measured by the CSU Na lidar from 0600 to 0700 UT is plotted in Fig. 5(a) along with the Mass

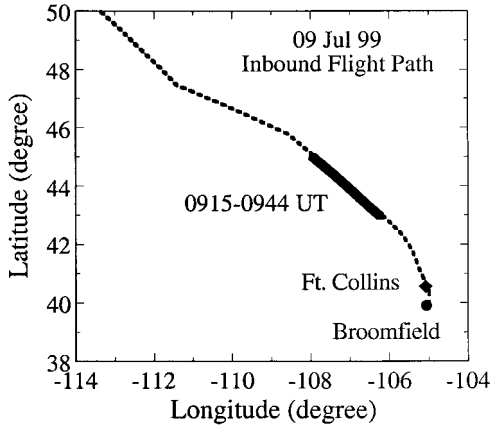

Fig. 4. Ground track of the 9 July 1999 flight path near Fort Collins and Broomfield, Colorado.

Spectrometer Incoherent Scatter Extended (MSISE-00) model and the temperature profile measured by the Fe lidar from 0915 to 0944 UT. The Fe density profiles are plotted in Fig. 5(b). The Fe densities are maximum at 85 km and are low for this time of year.

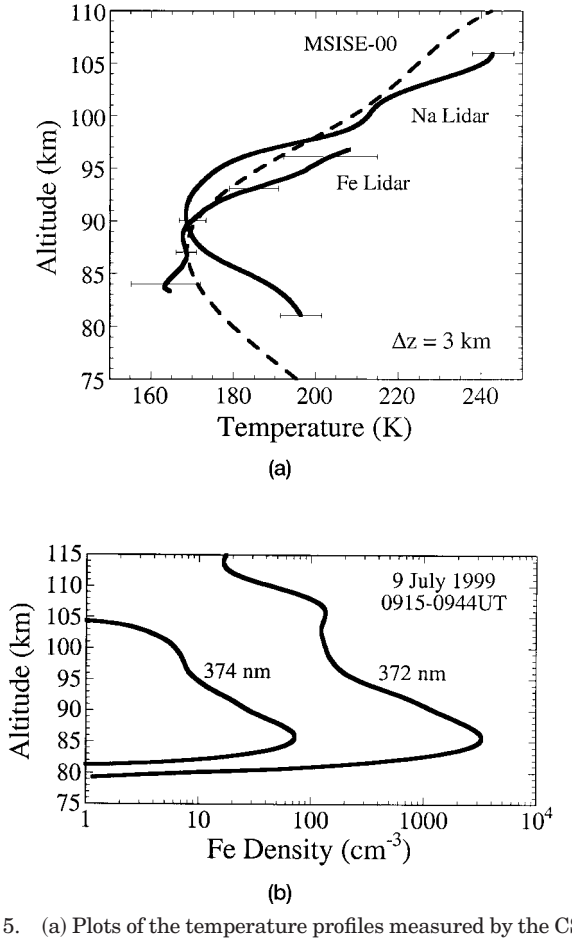

Fig. 5. (a) Plots of the temperature profiles measured by the CSU Na lidar and the airborne Fe lidar on the early morning of 9 July 1999 along with the MSISE-00 model at (40.6 °N, 105 °W) at 630 UT. (b) Plots of the 372- and 374-nm ground-state Fe density profiles measured by the airborne Fe lidar.

The Fe abundance (2.4×10^9 cm^{-2} at 372 nm) is approximately a factor of 2 lower than that observed at mid-summer at Urbana, Illinois (40 °N).[8]

We chose this period for comparison to avoid the aircraft descent into Broomfield. Although the observation periods are separated by 3 h and the Fe data were collected more than 400 km to the northwest of Fort Collins, the two data sets exhibit similar structure and comparable temperatures. The Fe temperature profile averages 2.2 K warmer than the Na profile between 83.3 and 96.8 km, and the rms difference between the two profiles is 14.8 K. Both profiles are consistent with the MSISE-00 model for this time of year and latitude. The 20-K differences between the Na and the Fe lidar measurements near 85 and 95 km are most likely due to tidal and gravity wave perturbations. Changes of 20 K or more over periods of a few hours are common at these altitudes.[10,11]

To determine if cross-section errors or, equivalently, laser linewidth errors, might be responsible for the differences between the Fe and the Na temperature profiles, the Fe data were reprocessed with different cross-section ratios. The minimum rms temperature difference is 14 K when the Fe data are processed with $R_\sigma = 1$. In this case the Fe temperature profile is 1.3 K colder than the Na profile. If we assume $\sigma_{L374} = 370$ MHz, $R_\sigma = 1$ implies $\sigma_{L372} = 435$ MHz. Although it is possible for the laser linewidths to differ by 65 MHz or approximately 18%, the minimum rms temperature difference is not significantly different from the result that uses the measured cross-section ratio (0.9325). For this reason, we believe that the differences in the Fe and Na temperature profiles are more likely due to the spatial separation and time difference of the observations rather than to lidar calibration errors.

7. North and South Pole Observations

The mesospheric Fe layer typically extends from approximately 80- to 100-km altitude with sporadic Fe (Fe_s) layers sometimes observed at altitudes as high as 115 km. The layer is created by meteoric ablation and depleted at its lower boundary by chemical processes. Fe chemistry is temperature dependent. The primary sink reaction $FeO + O_2 \rightarrow FeO_3$ on the layer's bottom side proceeds most rapidly at low temperatures.[12] This reaction drives the seasonal variations in the Fe column abundance.[8,13] Lidar observations at Urbana, Illinois, (40 °N) have revealed that the Fe abundance varies from a summertime low of $\sim 5 \times 10^9$ cm^{-2} to a wintertime high of $\sim 15 \times 10^9$ cm^{-2} with an annual mean of $\sim 11 \times 10^9$ cm^{-2}. Because mesopause temperatures are extremely low over the polar caps at mid-summer, the Fe densities are also expected to be quite low. Existing models predict peak densities of approximately 10^3 cm^{-3} compared with several times that value at mid-latitudes (J. Plane, School of Environmental Sciences, University of East Anglia, Norwich, NR4 7TJ, United Kindgom, personal communication, 1999). Thus summertime observations over the polar caps,

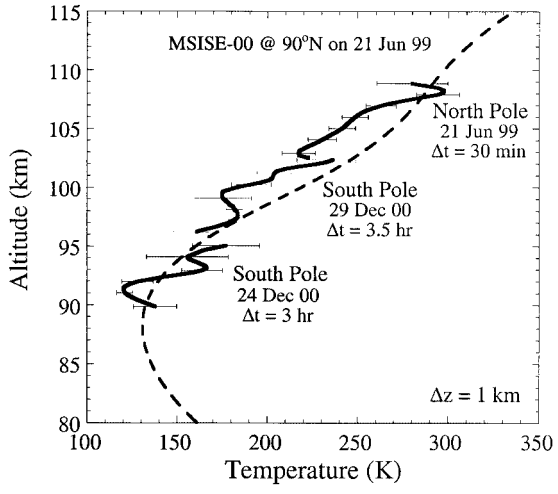

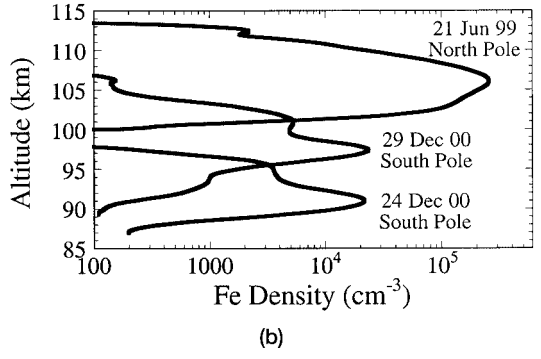

Fig. 6. (a) Temperature profiles measured by Fe Boltzmann temperature lidar over the North Pole on 21 June 1999 and over the South Pole on 24 December 2000 and 29 December 2000 along with MSISE-00 model data for 21 June 1999 at the North Pole. (b) The 372-nm ground-state Fe density profiles corresponding to the temperature profiles plotted in Fig. 6(a).

which are sunlit 24 h per day, represent the greatest challenge to making accurate temperature measurements with the Fe Boltzmann lidar.

A total of 52 h of airborne Fe lidar observations were conducted during the Arctic Mesopause Temperature Study described in Section 6. Four flights were made to the North Pole from Resolute Bay in late June and early July 1999. In November 1999 the lidar system was installed in the Atmospheric Research Observatory 488 m north of the geographic South Pole. Observations began on 2 December 1999. More than 800 h of measurements have been made at the South Pole through July 2001. A composite profile of temperatures measured during the summer solstice periods over the North and South Poles is plotted in Fig. 6(a). The corresponding Fe density profiles are plotted in Fig. 6(b). During midsummer over the polar caps, the Fe layer is thin, and the peak densities are typically quite low. The 21 June 1999 data over the North Pole are a notable exception. On this flight a sporadic Fe layer formed near 106 km in the lower thermosphere with peak densities exceeding 2×10^5 cm^{-3}. This prominent feature was observed on the three subsequent flights to the North Pole. However, the peak densities and abundances of the Fe_s on these later flights were much smaller. This dense sporadic layer provided an exceptionally strong backscatter signal so that excellent temperature data were obtained between 102 and 109 km. The thin layers observed at the South Pole near 91 km on 24 December 2000 and 98 km on 29 December 2000 are also sporadic layers, but the lower densities just above them are more typical. The combination of low densities and high background noise make temperature observations difficult at mid-summer over either pole. Even so, these airborne and ground-based profiles demonstrate that the lidar is capable of making useful temperature measurements, even in the daytime, whenever Fe densities (at 372 nm) are at least a few thousand atoms per cubic centimeter[3]. The Fe column abundances at both the 372- and 374-nm ground states for all the observations reported here are summarized in Table 5.

The polar regions are more sensitive than elsewhere to global change effects associated with greenhouse gas warming. Profiles of atmospheric parameters and constituents at the geographic poles can provide a convenient means of validating and calibrating global circulation models. However, measurements of key parameters, such as temperature profiles, have been conducted in only the troposphere and lower stratosphere at the geographic poles with balloon-borne sensors to altitudes less than 30 km. A major goal of the South Pole observations is to characterize the atmospheric temperature profile from the surface to the edge of space throughout the year. Plotted in Fig. 7(a) is a composite temperature profile determined by use of balloon and Fe/Rayleigh lidar data collected on 8 May 2000 that illustrates this capability. The corresponding Fe density profiles are plotted in Fig. 7(b). On that fall night it was possible to derive Fe temperatures in the lower thermosphere to as much as 110 km because of the presence of a high-altitude Fe_s layer. The lower mesosphere is approximately 20 K

Table 5. Fe Column Abundances for 372 and 374 nm

Date	21 June 1999	9 July 1999	8 May 2000	24 December 2000	29 December 2000
Location	North Pole	Fort Collins	South Pole	South Pole	South Pole
Duration	30 min	30 min	2 h	3 h	3.5 h
Abundance 372 nm (cm^{-2})	123.3×10^9	2.4×10^9	10.5×10^9	6.7×10^9	7.3×10^9
Abundance 374 nm (cm^{-2})	92.3×10^8	0.53×10^8	4.3×10^8	0.6×10^8	0.2×10^8

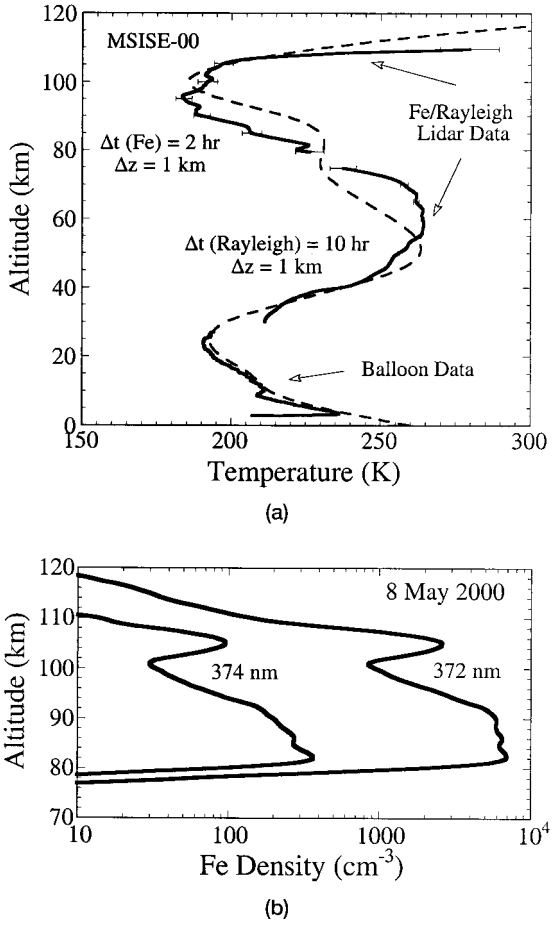

Fig. 7. (a) Composite temperature profile measured over the South Pole on 8 May 2000 by use of balloon and Fe–Rayleigh lidar data along with the MSISE-00 model for 8 May 2000 at the South Pole. (b) Plots of the 372- and 374-nm ground-state Fe density profiles.

warmer, and the upper mesosphere is approximately 20 K colder than predicted by the MSISE-00 model. More extensive data on the North Pole and South Pole measurements as well as seasonal and diurnal variations of the South Pole polar mesospheric clouds near 85-km altitude can be found in Ref. 14–16.

8. Discussion

The Fe Boltzmann technique is one of four lidar techniques that have been developed to measure temperature profiles in the middle and upper atmosphere. The Rayleigh technique, which depends on the relatively weak molecular scattering, requires a power aperture product of several hundred Wm^2 to make useful temperature measurements at altitudes near 100 km.[17] This requires 4-m class telescopes and 10–20-W lasers. Although achievable, it is unlikely these systems will be deployed to remote locations such as the South Pole any time soon, and they certainly cannot be deployed on aircraft. The narrow-band Na technique currently provides the highest resolution and most accurate temperature measurements of any system.[18,19] The combination of relatively high Na densities and large backscatter cross section yields strong signals even with a relatively modest telescope of a few tens of centimeters in diameter. Unfortunately, the sophisticated laser technology requires a laboratory environment to maintain proper operating conditions. Na systems cannot be easily deployed at remote sites and cannot be used for airborne observations. Because of the relatively low laser power (1–2 W), the molecular signal from Na lidars can be used to derive Rayleigh temperatures only to altitudes of 50–60 km. Narrow-band K systems based on solid-state alexandrite lasers operating in a pulsed ring configuration have been shown to be rugged enough to be deployed on ships and to provide good nighttime temperature profiles.[20] It is likely that these systems could also be deployed at remote sites and on aircraft. However, typical K densities are only 50–100 cm^{-3} so that the signal levels are weak, which makes daytime observations difficult. Because the K resonance line is in the near IR region of the spectrum, the molecular scattering is weak, and so the Rayleigh temperature capabilities of K lidars are limited to approximately 50 km.

As we have demonstrated, the Fe Boltzmann temperature lidar is rugged enough to be deployed at remote sites and provides exceptionally wide altitude coverage [see Fig. 7(a)]. The biggest drawback to the technique is the fact that the system is actually two complete lidar systems operating at 372 and 374 nm. The signal levels on the weak 374-nm channel limit the performance of the system. Typical Fe densities in this ground state at the peak of the layer vary from approximately 50 to 300 cm^{-3} so that daytime observations are doable but challenging and require long integration times. The observations presented in this paper, conducted near the summer solstice over the North and South Poles when the Fe densities are minimum and the background noise from the daytime sky is maximum, provided the toughest environmental tests of the instrument. In these first field campaigns, the impressive measurement capabilities of the Fe lidar have been demonstrated under the most extreme operating conditions. The lidar will remain until 1 November 2001 at the South Pole, where it is being used to characterize the seasonal variations of the temperature structure from 30 to 100 km, the Fe and Fe_s layer structure in the mesopause region and lower thermosphere, and polar mesospheric clouds near 85 km.

The authors gratefully acknowledge John Walling and his colleagues at Light Age, Inc., the NCAR flight crew, and the staff of the Amundsen–Scott South Pole Station for their superb support. We also acknowledge Robert Farley of The Aerospace Corporation for building the lidar-receiving telescopes and detector subsystems and Ashraf El Dakrouri for helping to install and operate the lidar at the South Pole. We thank C. Y. She and his group at Colorado State University for providing the Na lidar temperature data. We offer special thanks to Sunanda Basu and

John Lynch at the NSF for their encouragement and support in developing the Fe lidar and deploying it to the North and South Poles. This project was supported in part by NSF grants ATM 96-12251, ATM 97-09921, and OPP 96-16664.

References

1. G. E. Thomas, "Mesospheric clouds and the physics of the mesopause region," Rev. Geophys. **29,** 553–575 (1991).
2. C. S. Gardner and G. C. Papen, "Mesospheric Na wind/temperature lidar," Laser Rev. **23,** 131–134 (1995).
3. J. Sugar and C. Corliss, "Atomic energy levels of the iron-period elements: potassium through nickel," J. Phys. Chem. Ref. Data **14,** Suppl. 2 (1985).
4. J. A. Gelbwachs, "Iron Boltzmann factor LIDAR: proposed new remote-sensing technique for mesospheric temperature," Appl. Opt. **33,** 7151–7156 (1994).
5. C. S. Gardner, "Sodium resonance fluorescence lidar applications in atmospheric science and astronomy," Proc. IEEE **77,** 408–418 (1989).
6. J. R. Fuhr, G. A. Martin, and W. L. Wiese, "Atomic transition probabilities—iron through nickel," J. Phys. Chem. Ref. Data **17,** Suppl. 4 (1988).
7. G. C. Papen and D. Treyer, "Comparison of an Fe Boltzmann temperature lidar with a Na narrow-band lidar," Appl. Opt. **37,** 8477–8481 (1998).
8. T. J. Kane and C. S. Gardner, "Structure and seasonal variability of the nighttime mesospheric Fe layer at mid-latitudes," J. Geophys. Res. **98,** 16875–16886 (1993).
9. X. Chu, W. Pan, G. Papen, C. S. Gardner, G. Swenson, and P. Jenniskens, "Characteristics of Fe ablation trails observed during the 1998 Leonid meter shower," Geophys. Res. Lett. **27,** 1807–1810 (2000).
10. R. J. States and C. S. Gardner, "Thermal structure of the mesopause region (80–115 km) at 40 °N latitude. Part I: Seasonal variations," J. Geophys. Res. **57,** 66–77 (2000).
11. R. J. States and C. S. Gardner, "Thermal structure of the mesopause region (80–115 km) at 40 °N latitude. Part II: Diurnal variations," J. Geophys. Res. **57,** 78–92 (2000).
12. R. J. Rollason and J. M. C. Plane, "The reactions of FeO with O_3, H_2, H_2O, O_2, and CO_2," Phys. Chem. **2,** 2335–2343 (2000).
13. M. Helmer, J. M. C. Plane, J. Qian, and C. S. Gardner, "A model of meteoric iron in the upper atmosphere," J. Geophys. Res. **103,** 10913–10926 (1998).
14. C. S. Gardner, G. C. Papen, X. Chu, and W. Pan, "First lidar observations of middle atmosphere temperatures, Fe densities, and polar mesospheric clouds over the North and South Poles," Geophys. Res. Lett. **28,** 1199–1202 (2001).
15. X. Chu, C. S. Gardner, and G. Papen, "Lidar observations of polar mesospheric clouds at South Pole: seasonal variations," Geophys. Res. Lett. **28,** 1203–1206 (2001).
16. X. Chu, C. S. Gardner, and G. Papen, "Lidar observations of polar mesospheric clouds at South Pole: diurnal variations," Geophys. Res. Lett. **28,** 1937–1940 (2001).
17. J. W. Meriwether, P. D. Dao, R. T. McNutt, W. Klemetti, W. Moskowitz, and G. Davidson, "Rayleigh lidar observations of mesosphere temperature structure," J. Geophys. Res. **99,** 16973–16988 (1994).
18. C. Y. She, S. Chen, Z. Hu, J. Sherman, J. D. Vance, V. Vasoli, M. A. White, J. Yu, and D. A. Krueger, "Eight-year climatology of nocturnal temperature and sodium density in the mesopause region (80 to 105 km) over Fort Collins, CO (41 °N, 105 °W)," Geophys. Res. Lett. **27,** 3289–3292 (2000).
19. X. Chu, A. Z. Liu, G. Papen, C. S. Gardner, M. Kelley, J. Drummond, and R. Fugate, "Lidar observations of elevated temperatures in bright chemiluminescent meteor trails during the 1998 Leonid shower," Geophys. Res. Lett. **27,** 1815–1818 (2000).
20. U. von Zahn and J. Höffner, "Mesopause temperature profiling by potassium lidar," Geophys. Res. Lett. **23,** 141–144 (1996).